Nano-Micro Letters

e-ISSN 2150-5551
CN 31-2103/TB

ARTICLE

https://doi.org/10.1007/s40820-022-00862-0

Cite as
Nano-Micro Lett.
(2022) 14:121

Received: 8 February 2022
Accepted: 12 April 2022
Published online: 3 May 2022

Operando Converting BiOCl into $Bi_2O_2(CO_3)_xCl_y$ for Efficient Electrocatalytic Reduction of Carbon Dioxide to Formate

Huai Qin Fu[1], Junxian Liu[1], Nicholas M. Bedford[2], Yun Wang[1], Joshua Wright[3], Peng Fei Liu[4], Chun Fang Wen[4], Liang Wang[1], Huajie Yin[1], Dongchen Qi[5], Porun Liu[1] ✉, Hua Gui Yang[4], Huijun Zhao[1] ✉

HIGHLIGHTS

- An *operando* synthetic approach was exemplified to enhance catalyst stability for efficient reduction of CO_2 to formate.
- A highly stable $Bi_2O_2(CO_3)_xCl_y$ electrocatalyst was synthesized by direct electrochemical conversion of BiOCl via a cathodic potential-promoted anion-exchange process under *operando* CO_2RR conditions.
- The surface Cl^- in $Bi_2O_2(CO_3)_xCl_y$ changes the *p*-orbital electron states to enhance the stability and alters the CO_2RR pathway to markedly reduce the energy barrier.

ABSTRACT Bismuth-based materials (e.g., metallic, oxides and subcarbonate) are emerged as promising electrocatalysts for converting CO_2 to formate. However, Bi^o-based electrocatalysts possess high overpotentials, while bismuth oxides and subcarbonate encounter stability issues. This work is designated to exemplify that the *operando* synthesis can be an effective means to enhance the stability of electrocatalysts under *operando* CO_2RR conditions. A synthetic approach is developed to electrochemically convert BiOCl into Cl-containing subcarbonate ($Bi_2O_2(CO_3)_xCl_y$) under *operando* CO_2RR conditions. The systematic *operando* spectroscopic studies depict that BiOCl is converted to $Bi_2O_2(CO_3)_xCl_y$ via a cathodic potential-promoted anion-exchange process. The *operando* synthesized $Bi_2O_2(CO_3)_xCl_y$ can tolerate − 1.0 V versus RHE, while for the wet-chemistry synthesized pure $Bi_2O_2CO_3$, the formation of metallic Bi^o occurs at − 0.6 V versus RHE. At − 0.8 V versus RHE, $Bi_2O_2(CO_3)_xCl_y$ can readily attain a FE_{HCOO^-} of 97.9%, much higher than that of the pure $Bi_2O_2CO_3$ (81.3%). DFT calculations indicate that differing from the pure $Bi_2O_2CO_3$-catalyzed CO_2RR, where formate is formed via a *OCHO intermediate step that requires a high energy input energy of 2.69 eV to proceed, the formation of $HCOO^-$ over $Bi_2O_2(CO_3)_xCl_y$ has proceeded via a *COOH intermediate step that only requires low energy input of 2.56 eV.

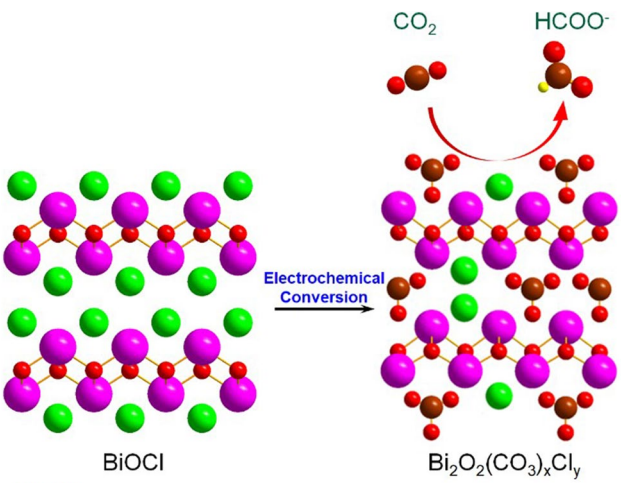

KEYWORDS Carbon dioxide reduction; Chloride-containing bismuth subcarbonate; Cathodic potential-promoted anion-exchange; Stability

✉ Porun Liu, p.liu@griffith.edu.au; Huijun Zhao, h.zhao@griffith.edu.au
[1] Centre for Catalysis and Clean Energy, Gold Coast Campus, Griffith University, Gold Coast, QLD 4222, Australia
[2] School of Chemical Engineering, University of New South Wales, Sydney, NSW 2052, Australia
[3] Department of Physics, Illinois Institute of Technology, Chicago, IL 60616, USA
[4] Key Laboratory for Ultrafine Materials of Ministry of Education, School of Materials Science and Engineering, East China University of Science and Technology, Shanghai 200237, People's Republic of China
[5] Centre for Materials Science, School of Chemistry and Physics, Queensland University of Technology, Brisbane, QLD 4001, Australia

1 Introduction

The renewable electricity-powered electrocatalytic carbon dioxide reduction reaction (CO_2RR) to produce chemicals/fuels not only curbs greenhouse gas emissions but also reduces our reliance on the rapidly diminished petroleum resources [1]. In this regard, various C_1 (e.g., carbon monoxide, formate, methane and methanol), C_2 and C_{2+} (e.g., ethylene, ethanol, acetylene, acetate, acetaldehyde, oxalic acid and *n*-propanol) CO_2RR products have been obtained [2, 3]. Among them, CO and $HCOO^-$/HCOOH are the most energy-efficient CO_2RR products as they can be formed by transferring two electrons to CO_2. Comparing to CO, converting CO_2 to $HCOO^-$/HCOOH is more desirable because $HCOO^-$/HCOOH are more valuable commodity chemicals [4, 5]. To date, the reported high-performance electrocatalysts for CO_2 reduction to $HCOO^-$/HCOOH are almost exclusively made of *p*-block metals-based materials such as In, Pb, Sn, Sb and Bi [6, 7].

Owning to their low toxicity and high selectivity toward $HCOO^-$/HCOOH, Bi-based CO_2RR electrocatalysts have attracted increasing attentions [8, 9]. Various Bi-based CO_2RR electrocatalysts such as metallic Bi^o, oxides and subcarbonate (Table S1) have been employed to electrocatalytically convert CO_2 to $HCOO^-$/HCOOH. As shown in Table S1, in general, the metallic Bi^o-based ones perform better than other forms of bismuth-containing electrocatalysts. Nevertheless, the metallic Bi^o-based electrocatalysts usually require high overpotentials, consequently the high cathodic potentials, to achieve their optimal performances [10, 11], undesirable for energy efficiency. In addition, high cathodic potentials are favorable for the competing hydrogen evolution reaction (HER), which often leads to low Faradic efficiencies toward $HCOO^-$/HCOOH (FE_{HCOO^-}/FE_{HCOOH}) [12]. The bismuth oxides-based electrocatalysts were also reported (Table S1). Noticeably, such electrocatalysts often encounter stability issues because the bismuth oxides in these electrocatalysts can be easily converted to metallic Bi^o under CO_2RR conditions [13]. For example, Deng et al. reported a Bi_2O_3 electrocatalyst with the optimal performance at − 0.9 V (vs RHE) to achieve a FE_{HCOO^-} of 91% with a partial $HCOO^-$ current density (J_{HCOO^-}) of ~ 8 mA cm^{-2} [14]. However, the as-synthesized Bi_2O_3 is found to be partially converted to metallic Bi^o under the CO_2RR conditions at − 0.9 V vs RHE. In fact, the reported bismuth oxides electrocatalysts require cathodic potentials ≥ − 0.9 (vs RHE) to concurrently achieve $FE_{HCOO^-} > 90\%$ with $J_{HCOO^-} \geq 15$ mA cm^{-2} [13, 15, 16]. Under such CO_2RR conditions, the bismuth oxides in these electrocatalysts are either partially or completely converted to metallic Bi^o. Other than metallic Bi^o and bismuth oxides, Zhang's group reported the use of ultrathin bismuth subcarbonate ($Bi_2O_2CO_3$) nanosheets to catalyze CO_2 reduction to $HCOO^-$ [17]. Their $Bi_2O_2CO_3$ electrocatalyst exhibits a very low overpotential of 610 mV and can achieve a FE_{HCOO^-} of 85% with a J_{HCOO^-} of ~ 11 mA cm^{-2} at − 0.7 V (vs HRE), however, partial conversion of $Bi_2O_2CO_3$ to the metallic Bi^o occurs within 30 min under − 0.65 V (vs RHE).

As reviewed above, under the required cathodic potentials to concurrently achieve high FE_{HCOO^-} and J_{HCOO^-}, the reported bismuth oxide and subcarbonate electrocatalysts are unavoidably reduced to metallic Bi^o, leading to the structural and compositional changes under *operando* CO_2RR conditions. Critically, such *operando* structural transformation processes are progressive and potential-dependent, leading to great difficulties to confirm the actual active sites, hence the catalysis mechanisms. Parenthetically, the synthetic conditions of the reported bismuth oxide and subcarbonate electrocatalysts are vastly different to their electrocatalytic application conditions, which could be a cause of their structural transformation under the *operando* CO_2RR conditions. If this is true, the severe *operando* stability issues might be effectively mitigated by employing identical synthesis and application conditions.

In this contribution, we report an approach to electrochemically convert bismuth oxychloride (BiOCl) into chloride-containing bismuth subcarbonate ($Bi_2O_2(CO_3)_xCl_y$) under *operando* CO_2RR conditions (at − 0.8 V vs RHE in CO_2-saturated 0.5 M $KHCO_3$ solution) and use it to exemplify that the *operando* synthesis can be an effective means to enhance the *operando* electrochemical stability of electrocatalysts. Systematic *operando* spectroscopic studies were conducted to depict the conversion mechanism and electrochemical stability. BiOCl is converted to $Bi_2O_2(CO_3)_xCl_y$ via the cathodic potential-promoted anion-exchange process. The obtained $Bi_2O_2(CO_3)_xCl_y$ can tolerate − 1.0 V versus RHE, while for the wet-chemistry synthesized pure tetragonal phased $Bi_2O_2CO_3$, the formation of metallic Bi^o occurs at − 0.6 V versus RHE, signifying a markedly improved electrochemical

 https://doi.org/10.1007/s40820-022-00862-0

stability. No notable structural change and performance decay are observed when $Bi_2O_2(CO_3)_xCl_y$ is subjected to the stability test at − 0.8 V versus RHE over a 20 h period. At − 0.8 V versus RHE, $Bi_2O_2(CO_3)_xCl_y$ can readily attain a FE_{HCOO^-} of 97.9%, much higher than that of $Bi_2O_2CO_3$ (81.3%). The density functional theory (DFT) calculations indicate that differing from $Bi_2O_2CO_3$-catalyzed CO_2RR, where HCOOH is formed via a *OCHO intermediate step that requires a high energy input energy of 2.69 eV to proceed, the formation of HCOOH over $Bi_2O_2(CO_3)_xCl_y$ has proceeded via a *COOH intermediate step that requires a notably reduced energy input of 2.56 eV.

2 Experimental and Calculation

2.1 Materials and Chemicals

Bismuth nitrate pentahydrate ($Bi(NO_3)_3{\cdot}5H_2O$, 99%), potassium chloride (KCl, 99.5%), ethanol (C_2H_5OH, 99%) and ethylene glycol ($C_2H_6O_2$, 99.8%) were purchased from ChemSupply. Urea (CH_4N_2O), Nafion (5 wt%) was purchased from Sigma-Aldrich. Carbon paper (TGP-H-060) and Nafion 115 proton exchange membrane were purchased from Alfa Aesar. The carbon paper was ultrasonically treated in deionized water and ethanol, followed by emerging in the concentrated HNO_3 at 100 °C for 12 h, thoroughly washed with the deionized water and ethanol and dried in air.

2.2 Synthesis of BiOCl-NSs

0.164 g of KCl and 0.868 g of $Bi(NO_3)_3{\cdot}5H_2O$ were dissolved in 70 mL H_2O and stirred for 1 h. The solution was transferred into a 100 mL Teflon-lined stainless-steel autoclave and kept at 120 °C for 24 h. The obtained BiOCl-NSs was adequately washed with deionized water and ethanol and dried at 60 °C for 6 h in vacuum oven.

2.3 Synthesis of $Bi_2O_2(CO_3)_xCl_y$

Twenty milligrams of the as-synthesized BiOCl-NSs was mixed with 80 μL Nafion solution (5 wt%) and dispersed 0.92 mL isopropanol under sonication for 40 min to form the ink. 100 μL ink was then cast onto the pre-treated carbon fiber paper substrate with an exposed area of 1×1 cm^2 (2 mg cm^{-2} of BiOCl-NSs). The carbon fiber paper with loaded BiOCl-NSs was used as the working electrode and subjected to − 0.8 V (vs RHE) in CO_2-saturated 0.5 M $KHCO_3$ solution for 2 h to electrochemically transform BiOCl-NSs to $Bi_2O_2(CO_3)_xCl_y$.

2.4 Synthesis of $Bi_2O_2CO_3$

For comparative purpose, pure $Bi_2O_2CO_3$ was synthesized. Under constant stirring, 0.234 g of $Bi(NO_3)_3{\cdot}5H_2O$ was dissolved into 10 mL H_2O, followed by adding 1.502 g of CH_4N_2O and 10 mL of C_2H_5OH. The resultant solution was then placed in the oil bath under 90 °C for 4 h. The obtained pure $Bi_2O_2CO_3$ was adequately washed with deionized water and ethanol and dried in a vacuum oven of 60 °C for 6 h.

2.5 Electrochemical Measurements

The electrochemical measurements were performed using a Nafion 115 proton exchange membrane separated two-compartment electrochemical cell consisting of a three-electrode system controlled by an electrochemical station (CHI 660E). For CO_2RR, the $Bi_2O_2(CO_3)_xCl_y$ working electrode (1×1 cm^2) was fabricated by operando electrochemical transformation of the immobilized BiOCl-NSs on carbon fiber paper, while the $Bi_2O_2CO_3$ working electrode was prepared by immobilizing 2 mg cm^{-2} of $Bi_2O_2CO_3$ on carbon fiber paper (1×1 cm^2). For all electrochemical measurements, an Ag/AgCl (3.5 M KCl) reference electrode, a Pt mesh counter electrode and CO_2-saturated 0.5 M $KHCO_3$ electrolyte (pH of 7.2) were employed. During CO_2RR, the electrolyte in the cathode compartment was constantly stirred at a rate of 800 rpm and bubbled with CO_2 at a flow rate of 5 mL min^{-1} controlled by a universal flow meter (Alicat Scientific, LK2). All reported potentials were converted to the reversible hydrogen electrode (RHE) in accordance with $E_{RHE} = E_{Ag/AgCl} + 0.059 \times pH + 0.205$. The gas chromatography (GC, RAMIN, GC2060) equipped with a flame ionization detector (FID) and a thermal conductivity detector (TCD) was used to qualitatively and quantitatively determine the gaseous products (e.g., H_2 and CO or other gaseous hydrocarbons). The CO and H_2 Faradaic efficiency were calculated as below:

$$FE_{CO} = 2x_{CO}pGF/IRT \quad (1)$$

$$FE_{H2} = 2x_{H2}pGF/IRT \quad (2)$$

where x_{CO} and x_{H2} (vol%) are the volume fractions of CO and H_2 in the exhaust gas, I (A) is the steady-state current, $G = 5$ mL min^{-1} is the CO_2 flow rate, $p = 1.013 \times 10^5$ Pa, $T = 273.15$ K, $F = 96{,}485$ C mol^{-1}, $R = 8.3145$ J mol^{-1} K^{-1}.

^{1}H nuclear magnetic resonance (^{1}H-NMR) was used to qualitatively and quantitatively determine the liquid phase products, including HCOOH. After reaction, 0.5 mL electrolyte from the cathode compartment was mixed with 0.1 mL D_2O containing 3-(trimethylsilyl)propanoic acid (TMSP) as the internal standard and subjected to NMR analysis. The Faradaic efficiency for formation of $HCOO^-$ was calculated as below:

$$FE = 2F \times n_{HCOO} - /(I \times t). \quad (3)$$

2.6 Characterizations

The morphologies and structures of the samples were characterized by SEM (JEOL JSM-7100) and TEM (Tecnai F20, 200 kV). The STEM images were recorded using a probe corrected JEOL JEM-ARM200F instrument with at an acceleration voltage of 200 kV. AFM measurements were performed using a Bruker Dimension Icon system. XRD patterns were collected from a Bruker D8 diffractometer. The *operando* XRD patterns were recorded using a Bruker D8 diffractometer and a home-made three-electrode electrochemical cell. Raman spectra were taken by a RENISHAW mVia Raman Microscope using a 532 nm excitation laser. The *operando* Raman studies were performed on a RENISHAW mVia Raman Microscope equipped with a microscopic lens immersed under the electrolyte to capture Raman signals and a home-made three-electrode electrochemical cell consisting of a BiOCl-NSs or $Bi_2O_2CO_3$ working electrode, an Ag/AgCl (3.5 M KCl) reference electrode and a Pt mesh counter electrode. The working electrodes were prepared by immobilizing BiOCl-NSs or $Bi_2O_2CO_3$ on a commercial Si substrate (1×1 cm^2). XPS spectra were recorded by Kratos Axis ULTRA using the C1 *s* at 284.8 eV as the internal standard. C and O K-edge XAS measurements were performed at the Soft X-ray spectroscopy beamline at Australian Synchrotron Facility, Australia's Nuclear Science and Technology Organisation (Clayton, Victoria, Australia). Bi L_3-edge XAS measurements were performed at the 10-ID-B beamline of the Advanced Photon Source (APS), Argonne National Laboratory (ANL). Data reduction, processing and subsequent modeling were performed using the Demeter XAS software package [18]. Modeling of the EXAFS data of $Bi_2O_2(CO_3)_xCl_y$ was performed using Bi–O, Bi–C and Bi–Bi backscattering paths from the crystal structure of $Bi_2O_2CO_3$ [19], while the Bi–Cl contributions were generated from the optimized structure generated from the DFT calculations. All EXAFS fitting was performed using an S_0^2 value of 0.868, which were obtained by modeling the EXAFS of a reference Bi foil (L_3-edge at 13,419 eV). To minimize error in CN and NND values, Debye–Waller factors were optimized in initial rounds of EXAFS fitting and then held constant.

2.7 DFT Calculations

All computation studies were performed using density functional theory (DFT) implemented in the Vienna Ab-initio Simulation Package (VASP) code in this study [20, 21]. For the effects of electron–electron exchange and correlation, the Perdew–Burke–Ernzerhof (PBE) functional at the generalized gradient approximation (GGA) level was employed [22]. The projected augmented wave (PAW) potentials were used throughout for ion–electron interactions [23], with the $5d^{10}6s^26p^3$, $2s^22p^2$, $2s^22p^4$, $3s^23p^5$ and $1s^1$ treated as valence electrons of Bi, C, O, Cl and H, respectively. The plane-wave cutoff of 520 eV was set for all the computations. The (1×2) clean {001} faceted $Bi_2O_2CO_3$ was modeled by a 14-atomic layer slab separated by a vacuum layer of 20 Å in this study. When geometries of all structures were optimized, top seven layers of the surfaces including adsorbate were relaxed, while the bottom seven layers were fixed. The gamma-centered Monkhorst–Pack *k*-point meshes with a reciprocal space resolution of $2\pi \times 0.04$ Å^{-1} were utilized for structural optimization. For the calculations on CO_2 and formic acid molecules, a $(20 \times 20 \times 20)$ Å^3 unit cell and a Γ-only *k*-point grid were used. All atoms were allowed to relax until the Hellmann–Feynman forces were smaller than 0.01 eV Å^{-1}, and the convergence criterion

https://doi.org/10.1007/s40820-022-00862-0

for the electronic self-consistent loop was set to 10^{-5} eV. The adsorption energy of each adsorbate [ΔE (eV/n)] was calculated as follows:

$$\Delta E = \frac{1}{n}\left(E_{ad/surf} - E_{surf} - nE_{ad}\right) \quad (4)$$

where E_{ad}, E_{surf} and $E_{ad/surf}$ are the energies of an adsorbate, the clean {001} facet and the surface with adsorbates, respectively. And n is the number of adsorbates on the surface.

Based on computational hydrogen electrode (CHE) model [24, 25], each electrochemical reaction step can be regarded as a simultaneous transfer of the proton–electron pair as a function of the applied potential. The reaction mechanism of CO_2 reduction should consist of the following elementary reactions:

$$CO_2(g) + * + H^+(aq) + e^- \rightarrow {}^*COOH \quad (5)$$

$${}^*COOH + H^+(aq) + e^- \rightarrow HCOOH + * \quad (6)$$

or

$$CO_2(g) + * + H^+(aq) + e^- \rightarrow {}^*OCHO \quad (7)$$

$${}^*OCHO + H^+(aq) + e^- \rightarrow HCOOH + * \quad (8)$$

where * means the corresponding surface and adsorbed states. The free energy for all intermediate states and non-adsorbed gas-phase molecule is calculated as:

$$G = E_{elec} + E_{ZPE} + \int C_p dT - TS \quad (9)$$

where the E_{elec} is the electronic energy obtained from DFT calculation; E_{ZPE} is the zero-point vibrational energy estimated by harmonic approximation; $\int C_p dT$ is the enthalpic correction and TS is the entropy. Here, reported values of E_{ZPE}, $\int C_p dT$ and TS are adopted [24]. The solvation effect has been considered for *COOH by stabilizing 0.25 eV [24].

3 Results and Discussion

3.1 Synthesis and Characterization of $Bi_2O_2(CO_3)_xCl_y$

In this work, $Bi_2O_2(CO_3)_xCl_y$ was synthesized by direct electrochemical conversion of the pre-synthesized BiOCl under *operando* CO_2RR conditions (Fig. 1a). The BiOCl nanosheets (BiOCl-NSs) were firstly synthesized as the precursor via a one-pot hydrothermal method [26]. The X-ray diffraction (XRD) pattern of the as-synthesized BiOCl-NSs (Fig. S1) can be indexed to the tetragonal BiOCl (PDF No. 06-0249). The Raman spectrum (Fig. S2) displays two strong peaks centered at 143 and 199 cm^{-1}, assignable to A^1_{1g} (external) and A^2_{1g} (internal) Bi–Cl vibration modes, respectively, while the weak peak at 400 cm^{-1} can be attributed to B^1_g mode [27]. The atomic force microscopy (AFM) and field-emission scanning electron microscopy (FE-SEM) images (Fig. S3a, b) disclose that the obtained BiOCl-NSs are octagonal shaped with sizes between 600 and 800 nm and thicknesses of ~ 150 nm. The high-resolution inverse fast Fourier transformation transmission electron microscopy (IFFT-TEM) image perpendicular to the nanosheet plane (Fig. S3c) reveals lattice spacings of 2.75 and 2.75 Å with an interplanar angle of 90°, corresponding to the (110) and ($\bar{1}$10) facets of BiOCl. The selected area electron diffraction (SAED) pattern (Fig. S3d) coincides to the diffraction pattern of the single crystal BiOCl ($k \pm l 0$, $k = l = n$) from [001] zone axis. The aberration-corrected high-angle annular dark-field scanning transmission electron microscopy (HAADF-STEM) image and the corresponding energy-dispersive X-ray spectroscopy (EDX) elemental mapping images confirm the homogeneous distribution of Bi, O and Cl throughout the entire BiOCl-NSs (Fig. S3e).

The as-synthesized BiOCl-NSs were then immobilized onto a conductive carbon paper substrate (1.0×1.0 cm^2) with a loading density of 2.0 mg cm^{-2} (Fig. S4) and subject to − 0.8 V (vs RHE) for 2 h in CO_2-saturated 0.5 M $KHCO_3$ solution to electrochemically convert the loaded BiOCl-NSs into $Bi_2O_2(CO_3)_xCl_y$. The XRD pattern (Fig. 1b) of the resultant $Bi_2O_2(CO_3)_xCl_y$ can be assigned to the tetragonal phased $Bi_2O_2CO_3$ (PDF No. 41–1488). The Raman spectrum (Fig. 1c) displays two strong peaks at 163 and 1068 cm^{-1}, attributing to the external vibration of $Bi_2O_2CO_3$ crystal and the ν_1 mode of the intercalated CO_3^{2-} between the $(BiO)_2^{2+}$ planes [28, 29]. Raman peak at 182 cm^{-1} could be assigned to the A_{1g} mode of the intercalated Cl^- in the interlayer [29, 30]. The FE-SEM and AFM images (Figs. 1d and S5) unveil that $Bi_2O_2(CO_3)_xCl_y$ possesses a sheeted structure with lateral sizes of 600–800 nm and thicknesses of 130–140 nm. The TEM image (Fig. 1e) shows that $Bi_2O_2(CO_3)_xCl_y$ is formed by multiple thin-layer structures with "doughnuts-like" shape, resulting from the substitution of chloride by carbonate. The SAED pattern normal to the nanosheets

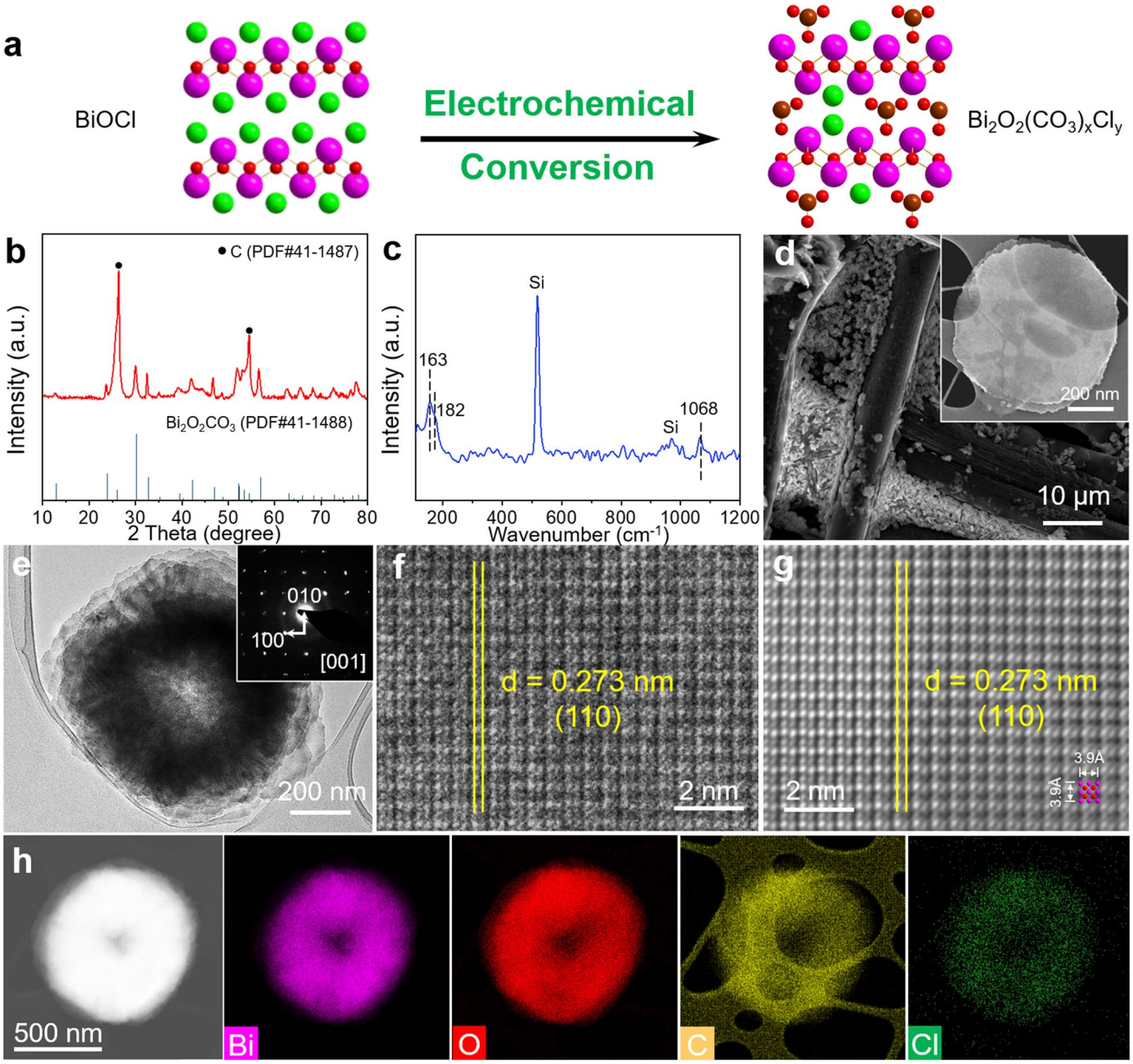

Fig. 1 **a** Schematic illustrating electrochemical conversion of BiOCl to $Bi_2O_2(CO_3)_xCl_y$ (Bi: pink, O: red, C: brown, Cl: green). **b** XRD pattern, **c** Raman spectrum, **d** FE-SEM images, **e** TEM image and SAED pattern, **f** HRTEM image, **g** IFFT-HRTEM image and **h** HAADF-STEM image and corresponding EDX element mapping images of $Bi_2O_2(CO_3)_xCl_y$ resulted from the electrochemical treatment of BiOCl-NSs under − 0.8 V versus RHE in CO_2-saturated 0.5 M $KHCO_3$ solution for 2 h. (Color figure online)

(inset of Fig. 1e) manifests the reflections of $Bi_2O_2CO_3$ ($k00$ and $0l0$, $k = l = n$) with [001] zone axis. The high-resolution TEM image (HRTEM, Fig. 1f) displays a lattice spacing of 0.273 nm, corresponding to $Bi_2O_2CO_3$ (110) plane, which is also confirmed by the high-resolution IFFT-HRTEM image (Fig. 1g). The HAADF-STEM image and the corresponding EDX elemental mapping (Fig. 1h) unveil the homogenously distributed Bi, O, C and Cl. The EDX estimated Bi/Cl atomic ratio in $Bi_2O_2(CO_3)_xCl_y$ is 17.7:1 (Fig. S6), significantly higher than that of BiOCl (1.2:1), confirming the presence of Cl in $Bi_2O_2(CO_3)_xCl_y$.

The X-ray photoelectron spectroscopy (XPS) analysis was then carried out. The high-resolution XPS Bi 4f spectra (Fig. 2a) confirm the presence of Bi^{3+} and Bi–O

 https://doi.org/10.1007/s40820-022-00862-0

bonds (160.0 and 165.3 eV) [31] in BiOCl. The Bi^{3+} peaks of $Bi_2O_2(CO_3)_xCl_y$ show a negative shift of 0.26 eV, consistent with that of reported $Bi_2O_2CO_3$ [32]. Figure 2b shows the high-resolution XPS O 1*s* spectra of BiOCl and $Bi_2O_2(CO_3)_xCl_y$. The former could be deconvoluted into the binding energy peaks assignable to the Bi–O lattice O (530.8 eV), the surface adsorbed hydroxyl (~ 531.9 eV) and O species in Nafion (536.3, 533.3 and 531.9 eV) [33, 34], while the deconvoluted binding energy peaks at 530.2 and 531.0 eV from the later are ascribed to the Bi–O lattice O and C=O, respectively [35, 36]. The lattice O peaks in $Bi_2O_2(CO_3)_xCl_y$ shifted to lower energies due to the substitution of chloride by carbonate. The two binding energy peaks at 199.2 and 200.8 eV assignable to Cl $2p_{3/2}$ and Cl $2p_{1/2}$ can be deconvoluted from the high-resolution XPS Cl 2*p* spectra of both BiOCl and $Bi_2O_2(CO_3)_xCl_y$ (Fig. 2c), indicating the presence of the lattice Cl^- [37]. Notably, a Bi/Cl atomic ratio of 61.5:1 is determined from the XPS Cl 2*p* spectrum of $Bi_2O_2(CO_3)_xCl_y$ (Fig. S7), confirming the presence of chemically bonded Cl on the surface of $Bi_2O_2(CO_3)_xCl_y$.

The X-ray absorption spectroscopy (XAS) measurements were then conducted to probe the electronic structure and local atomic environments. The O K-edge near-edge X-ray absorption fine structure (NEXAFS) spectra of BiOCl, $Bi_2O_2(CO_3)_xCl_y$ and reference samples are shown in Fig. 2d. The observed binding energy peaks at 532.0 and 537.0 eV from $Bi_2O_2(CO_3)_xCl_y$ are assignable to the hybridization of O 2*p* with Bi 6 *s* orbitals [38, 39], while the binding energy peak at 534 eV corresponds to the π^* C=O transition, indicating the presence of lattice carbonyl oxygen species [40]. The displayed binding energy peaks at 539.4 and 543.2 eV in the spectrum of $Bi_2O_2(CO_3)_xCl_y$ are ascribed to the non-equivalent σ^* C–O bonds in the carboxylic group originated from the adsorbed carbonate [41]. Based on the C K-edge NEXAFS spectra of $Bi_2O_2(CO_3)_xCl_y$ and reference samples (Fig. 2e), the binding energy peak at 289.5 eV can be attributed to the σ^* states of C–O [41], while the peaks at 297.2 and 299.8 eV are assignable to the σ^* C=O resonances associated with the presence of carbonate species [42]. It is to note that the O K-edge and C K-edge NEXAFS spectra obtained from $Bi_2O_2CO_3$ and $Bi_2O_2(CO_3)_xCl_y$ exhibit very similar characteristics, implying that the crystal structure of $Bi_2O_2CO_3$ in $Bi_2O_2(CO_3)_xCl_y$ is not noticeably altered by the presence of Cl^-. According to the Bi L_3-edge X-ray absorption near-edge structure (XANES) spectra (Fig. 2f), the same valence states of Bi^{3+} exist in BiOCl, $Bi_2O_2CO_3$ and $Bi_2O_2(CO_3)_xCl_y$. Figure 2g shows the k^2-weighted Fourier transformed Bi L_3-edge extended X-ray absorption fine structure (k^2-weighted FT-EXAFS) spectra of $Bi_2O_2CO_3$ and $Bi_2O_2(CO_3)_xCl_y$. The peaks at 1.74, 2.33 and 3.58 Å assignable to the Bi–O and Bi–Bi bonds in the $(BiO)_2^{2+}$ *ab* plane are observed from both $Bi_2O_2CO_3$ and $Bi_2O_2(CO_3)_xCl_y$, indicating an identical $(BiO)_2^{2+}$ *ab* plane in both $Bi_2O_2CO_3$ and $Bi_2O_2(CO_3)_xCl_y$. The spectrum of $Bi_2O_2CO_3$ shows a peak at 2.93 Å, corresponding to the interactions of Bi in $(BiO)_2^{2+}$ *ab* plane with the intercalated CO_3^{2-} between the $(BiO)_2^{2+}$ *ab* plane layers (the interlayer). Notably, for $Bi_2O_2(CO_3)_xCl_y$, the peak is shifted to 3.01 Å, implying the differences in the interactions of Bi in $(BiO)_2^{2+}$ *ab* plane with the interlayer anions due to the presence of the intercalated Cl^- in the interlayer of $Bi_2O_2(CO_3)_xCl_y$. The fittings of the Bi L_3-edge k^2-weighted FT-EXAFS spectra of $Bi_2O_2(CO_3)_xCl_y$ and $Bi_2O_2CO_3$ in *R* space and *k* space were then performed (Figs. 2h, S8 and Table S2) [43]. It unveils that the spectrum of $Bi_2O_2(CO_3)_xCl_y$ fits well with $Bi_2O_2CO_3$ and Bi–Cl path, confirming the presence of the intercalated Cl^- in the interlayer. The coordination numbers (CNs) of Bi–O in the first coordination sphere of $Bi_2O_2(CO_3)_xCl_y$ and $Bi_2O_2CO_3$ are 2.34 at 2.22 Å and 2.27 at 2.24 Å, respectively, further confirming an almost unchanged $(BiO)_2^{2+}$ *ab* plane coordination environment. For $Bi_2O_2CO_3$, a Bi–C CN of 1.75 at 3.36 Å represents the interactions between the Bi atoms in the $(BiO)_2^{2+}$ *ab* plane and the intercalated CO_3^{2-} in the interlayer. For $Bi_2O_2(CO_3)_xCl_y$, the measured Bi–C CN of 1.51 at 3.38 Å indicates a reduction in the Bi–C coordination. Notably, the fitting of the EXAFS spectrum of $Bi_2O_2(CO_3)_xCl_y$ using Bi–Cl backscattering path from the optimized structure corresponds to a Bi–Cl CN of 0.33, which is closely approximated to the dropped Bi–C CN, unambiguously confirming the presence of the intercalated Cl^- between $(BiO)_2^{2+}$ *ab* plane layers in $Bi_2O_2(CO_3)_xCl_y$. A likely $Bi_2O_2(CO_3)_xCl_y$ structure is shown in Fig. 2i. The above results confirm that under − 0.8 V (vs RHE) cathodic potential in CO_2-saturated 0.5 M $KHCO_3$ solution for 2 h, the BiOCl-NSs are electrochemically

3.2 *Operando* Converting BiOCl into $Bi_2O_2(CO_3)_xCl_y$

It is known that both of the tetragonal BiOCl and $Bi_2O_2CO_3$ crystals (Fig. S9) belong to the Sillén crystal family, featuring a matlockite-type positively charged

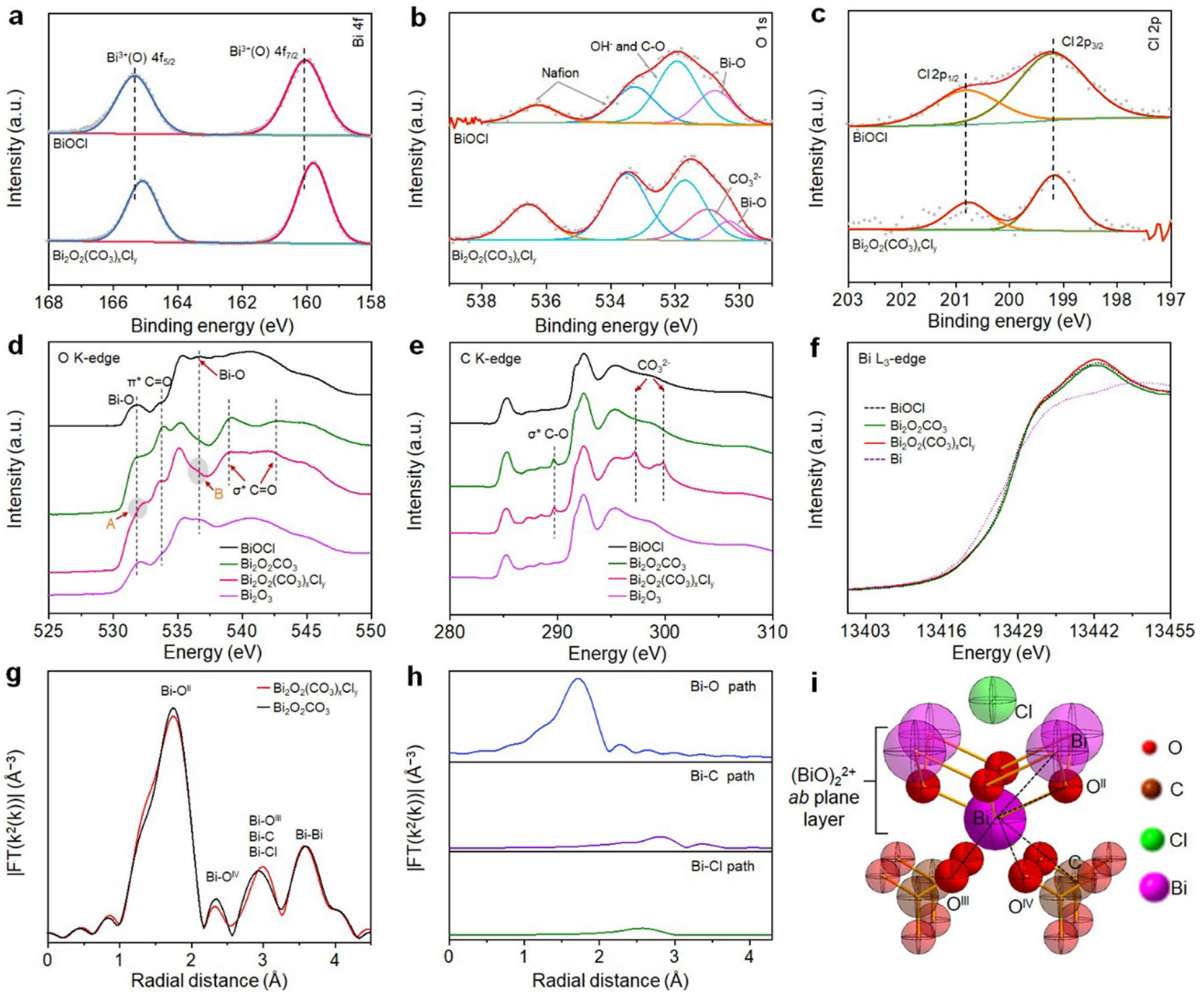

Fig. 2 High-resolution XPS spectra of **a** Bi 4f, **b** O 1*s* and **c** Cl 1*s* obtained from the as-synthesized BiOCl-NSs and $Bi_2O_2(CO_3)_xCl_y$. **d** O K-edge spectra, **e** C K-edge spectra and **f** Bi L_3-edge spectra of BiOCl, $Bi_2O_2CO_3$, $Bi_2O_2(CO_3)_xCl_y$ and referenced samples. **g** Bi L_3-edge k^2-weighted FT-EXAFS spectra of $Bi_2O_2(CO_3)_xCl_y$ and $Bi_2O_2CO_3$ in R space. **h** Fitting analysis of $Bi_2O_2(CO_3)_xCl_y$ using Bi–O, Bi–C and Bi–Cl paths. **i** Proposed geometric configuration of $Bi_2O_2(CO_3)_xCl_y$

$(BiO)_2^{2+}$ *ab* plane layer structure stacking between the negatively charged bichloride and "standing-on-end" CO_3^{2-} anions slabs, respectively. Comparing to the *d* spacing of {001} faceted BiOCl along the *c* axis (7.83 Å), the *d spacing* of {002} faceted $Bi_2O_2CO_3$ is markedly reduced to 6.84 Å. Therefore, under apt cathodic potentials, due to the layer structure similarity, and the apparently decreased *d* spacing of {002} faceted $Bi_2O_2CO_3$, the transformation of BiOCl to $Bi_2O_2CO_3$ could occur via the intercalative substitution of the interlayer Cl^- with CO_3^{2-} through a glide of the neighboring $(BiO)_2^{2+}$ *ab* planes along [100] and [010] directions with the translational distances of ½ *a* and ½ *b*, respectively [17]. To depict the structural evolution processes under the *operando* CO_2RR conditions, the BiOCl-NSs immobilized on the carbon fiber paper were subjected to different cathodic potentials (E_{App}) in CO_2-saturated 0.5 M $KHCO_3$ solution, and the XRD patterns were *operando* recorded. The XRD patterns recorded under the open circuit potential (OCP) and $E_{App} \leq -0.2$ V (Fig. 3a) are almost identical to that of the as-synthesized BiOCl (Fig. S1). The initial conversion of BiOCl to $Bi_2O_2(CO_3)_xCl_y$ occurs at $E_{App} = -0.3$ V as

 https://doi.org/10.1007/s40820-022-00862-0

indicated by the observed diffraction peak at 56.9° corresponding to {123} faceted $Bi_2O_2CO_3$. When E_{App} is increased from − 0.3 to − 0.7 V, although the recorded XRD patterns are still dominated by the diffraction patterns of BiOCl, the progress of converting BiOCl to $Bi_2O_2(CO_3)_xCl_y$ is evidenced by the progressively increased intensities of $Bi_2O_2CO_3$ diffraction peaks and the accompanied decrease in the intensities of BiOCl diffraction peaks. With $E_{App} = -$ 0.8 V, all recorded diffraction peaks belong to $Bi_2O_2CO_3$ (PDF No. 41-1488), signifying the complete conversion of BiOCl to $Bi_2O_2(CO_3)_xCl_y$. The structural evolution and the time required to completely convert BiOCl to $Bi_2O_2(CO_3)_xCl_y$ under $E_{App} = -$ 0.8 V were subsequently investigated (Fig. S10). As can be seen, BiOCl is fully covered to $Bi_2O_2(CO_3)_xCl_y$ within 60 min under $E_{App} = -$ 0.8 V. As disclosed in Fig. 3a, $Bi_2O_2(CO_3)_xCl_y$ remains as the sole product when $-0.8\ V \le E_{App} \le -1.0\ V$. With $E_{App} = -$ 1.1 V, the bismuth in $Bi_2O_2(CO_3)_xCl_y$ is partially reduced to the metallic phased Bi^o as evidenced by the appearance of the diffraction peaks assignable to rhombohedral phased Bi^o (PDF No. 05–0519). With $E_{App} = -$ 1.2 V, all of the recorded diffraction peaks belong to the rhombohedral phased Bi^o, confirming the ultimate conversion of $Bi_2O_2(CO_3)_xCl_y$ to the metallic Bi^o phase. As shown in Fig. S11, the BiOCl-derived Bi^o at $E_{App} = -$ 1.2 V is formed by the aggregated Bi^o NSs with the exposed {001} facets. Notably, the required cathodic potential to convert $Bi_2O_2(CO_3)_xCl_y$ to Bi^o is more negative than those reported potentials to reduce $Bi_2O_2CO_3$ to Bi^o [44], {Lv, 2017 #1765}inferring a superior electrochemical stability of $Bi_2O_2(CO_3)_xCl_y$ over $Bi_2O_2CO_3$, which might be attributed to the presence of Cl^- in $Bi_2O_2(CO_3)_xCl_y$. To confirm this, the pure tetragonal phased $Bi_2O_2CO_3$ nanosheets (Figs. S12–S14) were synthesized by a wet-chemistry method [43] and subjected to different cathodic potentials in CO_2-saturated 0.5 M $KHCO_3$ solution. Figure 3b shows the *operando* recorded XRD patterns. The formation Bi^o occurs at $E_{App} = -$ 0.6 V, while the $Bi_2O_2CO_3$ is fully converted to the rhombohedral phased metallic Bi^o (PDF No. 05-0519) at $E_{App} = -$ 0.8 V, confirming that the presence of Cl^- in $Bi_2O_2(CO_3)_xCl_y$ is responsible for the improved electrochemical stability. It is noteworthy that compared to the characteristic diffraction peaks of $Bi_2O_2CO_3$, all of the recorded characteristic diffraction peaks from $Bi_2O_2(CO_3)_xCl_y$ are shifted slightly toward lower angles (Fig. S15), indicating an expended *d* spacing in $Bi_2O_2(CO_3)_xCl_y$ due to the presence of Cl^- in the interlayer. The above *operando* XRD studies unveil that the electrochemical conversion of BiOCl to $Bi_2O_2(CO_3)_xCl_y$ is realized by the cathodic potential-promoted anion-exchange in the interlayer between the $(BiO)_2^{2+}$ *ab* planes.

To further elaborate the electrochemical conversion pathway, the *operando* potential-dependent Raman spectra of BiOCl immobilized on the carbon fiber paper were recorded under different cathodic potentials in CO_2-saturated 0.5 M $KHCO_3$ solution (Fig. 3c). Under the OCP and $E_{App} \le -$ 0.3 V conditions, the recorded spectra are almost identical to that of the as-synthesized BiOCl-NSs (Fig. S2). With $E_{App} = -$ 0.4 V, the characteristic peaks of BiOCl at 143 (A_{1g}^1) and 199 cm^{-1} (A_{1g}^2) are markedly reduced and disappeared, respectively, which are accompanied by the appearance of a new peak at 182 cm^{-1} that might be assigned to the A_{1g} mode of the intercalated Cl^- in the interlayer, although this could be complicated by the reduced crystal symmetry due to the disorder or free rotation of CO_3^{2-} in the interlayer [29, 30]. These observed changes in the Raman spectrum signify the initial conversion of BiOCl to $Bi_2O_2(CO_3)_xCl_y$ at $E_{App} = -$ 0.4 V, consistent with the *operando* XRD observation shown in Fig. 3a. At $E_{App} = -$ 0.8 V, two new peaks at 163 and 1068 cm^{-1} attributed to the external vibration of $Bi_2O_2CO_3$ crystal and the ν_1 mode of CO_3^{2-} anions between the $(BiO)_2^{2+}$ planes appear, signifying the complete conversion of BiOCl to $Bi_2O_2(CO_3)_xCl_y$. Within $-0.8\ V \le E_{App} \le -1.0\ V$, the peak at 182 cm^{-1} (A_{1g} mode) is rapidly decreased, while the peaks at 163 and 1068 cm^{-1} are evolved and intensified, which are likely due to the changes in the local atomic symmetry rather than the crystal cell parameters because of the unchanged *operando* XRD patterns within the same potential range (Fig. 3a). It is known that the high-intensity Raman bands between 150 and 200 cm^{-1} normally correspond to the out-of-plane lattice vibrations of the Bi atoms perpendicular to the $(BiO)_2^{2+}$ layers [45]. Because the phonon frequencies are sensitive to the dopant-induced asymmetry and the interlayer thickness, therefore, the blueshifted phonons from 182 to 163 cm^{-1} could be resulted from the suppressed vibrations of the $(BiO)_2^{2+}$ layers along *c* direction due to the replaced Cl^- by CO_3^{2-} at relatively high cathodic potentials. The characteristic Raman peaks of $Bi_2O_2CO_3$ at 163 and 1068 cm^{-1} are dramatically decreased under $E_{App} = -$ 1.1 V and vanished

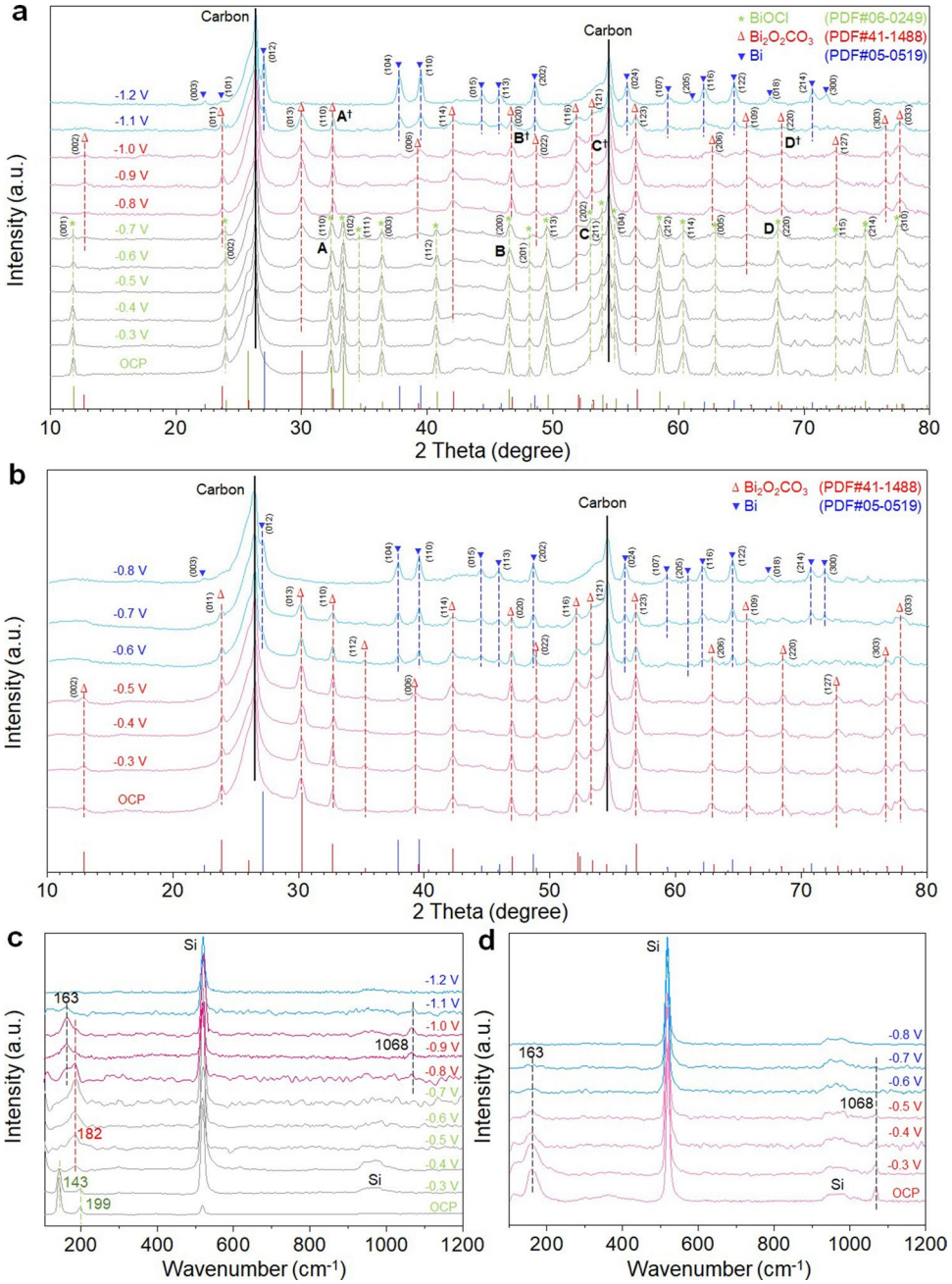

Fig. 3 **a**, **b** *Operando* XRD patterns of the as-synthesized BiOCl-NSs and $Bi_2O_2CO_3$ recorded from CO_2-saturated 0.5 M $KHCO_3$ solution under different cathodic potentials. **c**, **d** *Operando* Raman spectra of the as-synthesized BiOCl-NSs and $Bi_2O_2CO_3$ recorded from CO_2-saturated 0.5 M $KHCO_3$ solution under different cathodic potentials

at $E_{App} = -1.2$ V due to the formation of metallic Bi^o, consistent with the *operando* XRD observations. For comparative purpose, the *operando* potential-dependent Raman spectra of the pure tetragonal phased $Bi_2O_2CO_3$ nanosheets were obtained (Fig. 3d). When $E_{App} \leq -0.5$ V, the peak at 182 cm^{-1} associating with the A_{1g} mode of the intercalated Cl^- in the CO_3^{2-} slab is absent, while the characteristic Raman peaks of $Bi_2O_2CO_3$ at 163 and 1068 cm^{-1} are apparent, however, rapidly extinct when $E_{App} \geq -0.6$ V due to the formation of metallic Bi^o, consistent with the *operando*

 https://doi.org/10.1007/s40820-022-00862-0

XRD observations shown in Fig. 3b. This further confirms that compared to the chloride-free $Bi_2O_2CO_3$, the reduction of $Bi_2O_2(CO_3)_xCl_y$ to metallic Bi^o requires a much higher cathodic potential due to presence of the intercalated Cl^- in the CO_3^{2-} slab, signifying a noticeably improved electrochemical stability. These *operando* Roman studies further suggest that the conversion of BiOCl to $Bi_2O_2(CO_3)_xCl_y$ is achieved by the cathodic potential-promoted anion-exchange in the interlayer.

3.3 CO_2RR Performance

All electrochemical measurements were performed using a three-electrode electrochemical system with $Bi_2O_2(CO_3)_xCl_y$ or $Bi_2O_2CO_3$ working electrode in CO_2- or Ar-saturated 0.5 M $KHCO_3$ solution. When $E_{App} > -0.5$ V (vs EHE), the linear sweep voltammetry (LSV) responses of $Bi_2O_2(CO_3)_xCl_y$ in CO_2-saturated solution display higher cathodic current densities than that obtained from the Ar-saturated solution (Fig. S16), indicating a superior electrocatalytic activity of $Bi_2O_2(CO_3)_xCl_y$ toward CO_2RR. The potentiostatic experiments were then performed under different cathodic potentials to examine the electrocatalytic CO_2RR activity and selectivity. Figure 4a shows the chronoamperometric curves of $Bi_2O_2(CO_3)_xCl_y$ from the CO_2-saturated 0.5 M $KHCO_3$ solution. The reaction products in gaseous and aqueous phases were qualitatively identified and quantitatively determined by the gas chromatography (GC) and nuclear magnetic resonance (NMR). For all cases investigated, H_2 is identified as the sole product in the gaseous phase, while the formate is found to be the sole product in the aqueous phase. The NMR determined formate concentrations (Figs. S17 and S18) corresponding to the chronoamperometric curves shown in Fig. 4a were used to calculate the corresponding FE_{HCOO^-} and J_{HCOO^-} values. Figure 4b shows the plot of J_{HCOO^-} against E_{App}. For both $Bi_2O_2(CO_3)_xCl_y$ and $Bi_2O_2CO_3$, an increase in E_{App} leads to an increase in J_{HCOO^-}. For a given E_{App}, the observed J_{HCOO^-} from $Bi_2O_2(CO_3)_xCl_y$ is higher than that observed from $Bi_2O_2CO_3$, implying a superior CO_2RR activity of $Bi_2O_2(CO_3)_xCl_y$ over $Bi_2O_2CO_3$. At $E_{App} = -0.8$ V, the J_{HCOO^-} attained by $Bi_2O_2(CO_3)_xCl_y$ is 18.4 mA cm^{-2}, higher than that of $Bi_2O_2CO_3$ (14.2 mA cm^{-2}). Figure 4c shows the plot of FE_{HCOO^-} (derived from Fig. 4a) against E_{App}. For $Bi_2O_2(CO_3)_xCl_y$, an increase in E_{App} from − 0.4 to − 0.6 V leads to a rapidly increased FE_{HCOO^-} from 79.2 to 96.2%, and further increasing E_{App} to − 0.8 V leads to an increased FE_{HCOO^-} to 97.9%. FE_{HCOO^-} remains almost unchanged when E_{App} is further increased to − 1.0 V, while the corresponding J_{HCOO^-} is increased to 40.5 mA cm^{-2} (Fig. 4b). Based on the *operando* XRD and Raman observations (Fig. 3a, c), the formation of the metallic phased Bi^o will not occur with $E_{App} \leq -1.0$ V, therefore, the observed changes in FE_{HCOO^-} from the potential range of $-0.4\ V \leq E_{App} \leq -1.0$ V reflect the influence of potential on CO_2RR selectivity of $Bi_2O_2(CO_3)_xCl_y$. Although $Bi_2O_2(CO_3)_xCl_y$ is partially converted to metallic Bi–NSs within $-1.0\ V \leq E_{App} \leq -1.2$ V (Fig. 3a, c), the high FE_{HCOO^-} can still be attained due to the electrocatalytic activity of Bi^o toward CO_2RR under high cathodic potentials [17]. When $E_{App} > -1.2$ V, the observed decrease in FE_{HCOO^-} is due to the intensified competition from HER [7]. Interestingly, for pure $Bi_2O_2CO_3$, a rapidly increased FE_{HCOO^-} from 65.5 to 77.5% is observed when E_{App} is increased from − 0.4 to − 0.6 V and reached a maxima FE_{HCOO^-} of 83.0% at $E_{App} = -0.7$ V, where $Bi_2O_2CO_3$ is partially converted to the metallic Bi^o. With $-0.8\ V \leq E_{App} \leq -1.2$ V, $Bi_2O_2CO_3$ is fully converted to the metallic Bi^o and the slightly decreased FE_{HCOO^-} reflects the influence of potential on CO_2RR selectivity of metallic Bi^o rather than that of $Bi_2O_2CO_3$. When $E_{App} > -1.2$ V, FE_{HCOO^-} is rapidly decreased due to the intensified competition from HER.

The chronoamperometric stability of $Bi_2O_2(CO_3)_xCl_y$ (Fig. 4d) was evaluated over a 20 h period in CO_2-saturated 0.5 M $KHCO_3$ solution at $E_{App} = -0.8$ V vs RHE. While FE_{HCOO^-} of ~ 95% is well retained, a 12.1% increase in the cathodic current density is observed, indicating an increased J_{HCOO^-}. Interestingly, when the used electrolyte is replaced by the fresh one, an almost identical chronoamperometric curve is obtainable with ~ 12% increase in the cathodic current density at 20 h, indicating an excellent long-term stability of $Bi_2O_2(CO_3)_xCl_y$ [46]. The excellent electrocatalytic stability of $Bi_2O_2(CO_3)_xCl_y$ can be attributed to its excellent structural stability as evidenced by the almost unchanged XRD pattern (Fig. S19), Raman spectra (Fig. S20), as well as SEM and TEM images (Fig. S21) of $Bi_2O_2(CO_3)_xCl_y$ after the chronoamperometric stability test. The chronoamperometric stability of $Bi_2O_2CO_3$ was also evaluated at $E_{App} = -0.8$ V vs RHE (Fig. S22). Over a 20 h testing period, FE_{HCOO^-} is decreased from 86.2 to 80.0%, while the cathodic current density is increased from

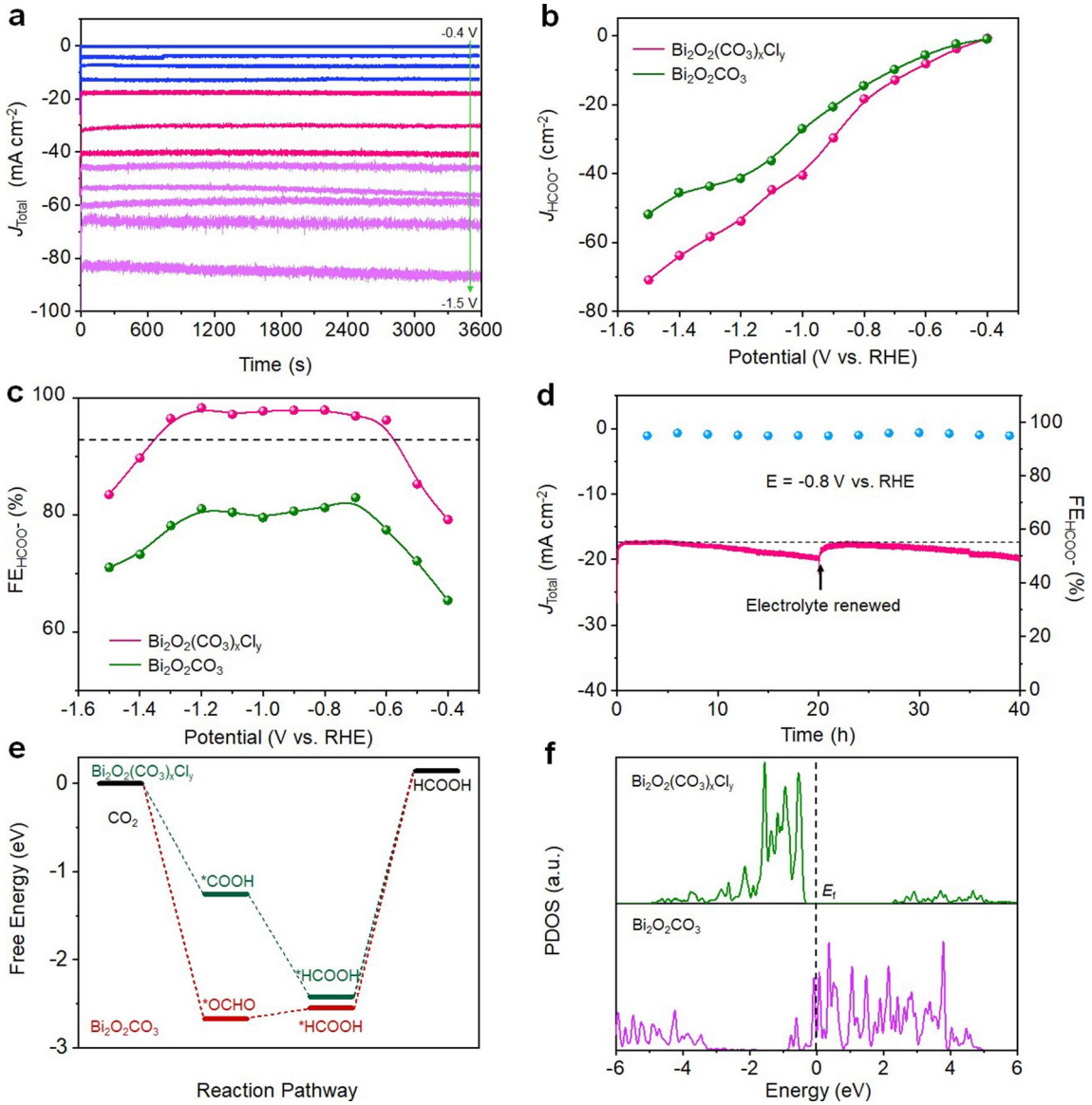

Fig. 4 **a** Chronoamperometric curves of $Bi_2O_2(CO_3)_xCl_y$ recorded from CO_2-saturated 0.5 M $KHCO_3$ solution under different cathodic potentials. **b**, **c** Plots of HCOOH partial current density and Faradic efficiency against catholic potential for $Bi_2O_2(CO_3)_xCl_y$- and $Bi_2O_2CO_3$-catalyzed CO_2RR. **d** Chronoamperometric curves and FE_{HCOOH} of $Bi_2O_2(CO_3)_xCl_y$ at − 0.8 V versus RHE. **e** Free energy diagrams of $Bi_2O_2(CO_3)_xCl_y$- and $Bi_2O_2CO_3$-catalyzed CO_2 reduction to HCOOH. **f** PDOSs plots of $Bi_2O_2(CO_3)_xCl_y$- and $Bi_2O_2CO_3$-catalyzed CO_2 reduction to HCOOH

12.5 to 14.2 mA cm^{-2}. However, after the chronoamperometric stability test, the pure tetragonal phased $Bi_2O_2CO_3$ is fully converted to the metallic phased Bi^o (Figs. S23–S26). The stability test result confirms that $Bi_2O_2(CO_3)_xCl_y$ fabricated under *operando* CO_2RR conditions possesses excellent stability.

3.4 DFT Calculations

It is known that electrocatalytic CO_2RR to HCOOH has normally proceeded via a proton-coupled electron transfer (PCET) step to form *COOH or *OCHO intermediates and followed by another PCET step to generate HCOOH [47]. It

https://doi.org/10.1007/s40820-022-00862-0

is also known that the CO_2RR pathway depends strongly on the adsorption energy of the intermediates [48]. DFT calculations were therefore carried out to determine the preferential intermediates of the pure tetragonal phased $Bi_2O_2CO_3$- and $Bi_2O_2(CO_3)_xCl_y$-catalyzed CO_2 reduction to HCOOH. Our DFT calculations unveil that *OCHO intermediate can preferentially adsorb on the {001} faceted Cl-free $Bi_2O_2CO_3$ surface [49] with an adsorption free energy (ΔG_{*OCHO}) of − 2.67 eV (Fig. S27a), while no stable structure of *COOH intermediate adsorbed on the {001} faceted Cl-free $Bi_2O_2CO_3$ can be obtained. These results imply that the pure tetragonal phased $Bi_2O_2CO_3$-catalyzed CO_2 reduction to HCOOH has proceeded via a *OCHO intermediate pathway. In contrast, our initial DFT calculations are failed to obtain a stable structure of *OCHO intermediate adsorbed on $Bi_2O_2(CO_3)_xCl_y$ surface. Nonetheless, further DFT calculations unveil that the *COOH intermediate is apt to absorb to the $Bi_2O_2(CO_3)_xCl_y$ surface with a ΔG_{*COOH} of − 1.25 eV (Fig. S27b), inferring that the $Bi_2O_2(CO_3)_xCl_y$-catalyzed CO_2 reduction to HCOOH has proceeded via a *COOH intermediate pathway. Figure 4e illustrates the free energy diagrams of $Bi_2O_2CO_3$- and $Bi_2O_2(CO_3)_xCl_y$-catalyzed CO_2 reduction to HCOOH. During the 1st PCET step, the formation of *OCHO on $Bi_2O_2CO_3$ surface and *COOH on $Bi_2O_2(CO_3)_xCl_y$ surface is exothermic. During the 2nd PCET step, the formation of *HCOOH on $Bi_2O_2(CO_3)_xCl_y$ is exothermic, while on $Bi_2O_2CO_3$ is endothermic. The desorption of *HCOOH from $Bi_2O_2CO_3$ and $Bi_2O_2(CO_3)_xCl_y$ to form HCOOH are energetically uphill. However, the desorption of *HCOOH from $Bi_2O_2(CO_3)_xCl_y$ requires 2.56 eV to proceed, which is 0.13 eV lower than that of $Bi_2O_2CO_3$ (2.69 eV), indicating a better kinetic activity of $Bi_2O_2(CO_3)_xCl_y$ over the Cl-free $Bi_2O_2CO_3$. The poor kinetic activity of $Bi_2O_2CO_3$ could be resulted from the excessively high adsorption energy of *OCHO impeded active sites turnover. Figure 4f shows the projected density of states (PDOS) of the *p* bands of Bi sites in $Bi_2O_2(CO_3)_xCl_y$ and the {001} faceted $Bi_2O_2CO_3$. As can be seen, the PDOS of the {001} faceted $Bi_2O_2CO_3$ near Fermi level is dominated by the *p*-orbital electron states with much higher electronic densities than that of $Bi_2O_2(CO_3)_xCl_y$, indicating a higher reactivity for *OCHO intermediate adsorption, hence an impeded active sites regeneration [50, 51]. In addition, the high PDOS density of the {001} faceted $Bi_2O_2CO_3$ near Fermi level indicates high densities of the unoccupied *p*-orbital states of Bi in the {001} faceted $Bi_2O_2CO_3$ with an estimated lowest unoccupied molecular orbital (LUMO) energy of 0.4 eV above Fermi level, corresponding to a LUMO potential of − 0.4 eV. In strong contrast, for $Bi_2O_2(CO_3)_xCl_y$, the *p*-orbital electron states can only be observed at 2.3 eV above the Fermi level with low densities, indicating low unoccupied *p*-orbital states of Bi in $Bi_2O_2(CO_3)_xCl_y$, corresponding to a LUMO potential of − 2.3 eV. It is known that for semiconductor electrodes, the reduction reaction takes place via the injection of electrons into LUMO. Therefore, the LUMO potential corresponds to the minimum required cathodic potential for electron injection. As illustrated in Fig. S28, compared to $Bi_2O_2CO_3$, the higher LUMO potential of $Bi_2O_2(CO_3)_xCl_y$ infers that a higher cathodic potential is required to convert Bi^{3+} in $Bi_2O_2(CO_3)_xCl_y$ to metallic Bi^o, which explains the superior electrochemical stability of $Bi_2O_2(CO_3)_xCl_y$ over $Bi_2O_2CO_3$ under CO_2RR conditions.

4 Conclusions

In summary, we reported an approach to electrochemically convert bismuth oxychloride (BiOCl) into chloride-containing bismuth subcarbonate ($Bi_2O_2(CO_3)_xCl_y$) under *operando* CO_2RR conditions. We demonstrated that the *operando* synthesis is an effective strategy to enhance the electrochemical stability of bismuth-based electrocatalysts. The exemplified approach in this work could be widely applicable to enhance the electrochemical stabilities of other electrocatalysts for other reactions.

Acknowledgements This work was financially supported by Australian Research Council Discovery Project (DP200100965). Bi L_3-edge XAS measurements were performed at the 10-ID-B beamline of the Advanced Photon Source, a U.S. Department of Energy (DOE) Office of Science User Facility, operated for the DOE Office of Science by Argonne National Laboratory under Contract No. DE-AC02-06CH11357. Operations at 10-ID-B are further supported by members of the Materials Research Collaborative Access Team. C and O K-edge measurements were performed at the SXR beamline of the Australian Synchrotron, part of the Australian Nuclear Science and Technology Organisation.

Funding Open access funding provided by Shanghai Jiao Tong University.

Supplementary Information The online version contains supplementary material available at https://doi.org/10.1007/s40820-022-00862-0.

References

1. P.D. Luna, C. Hahn, D. Higgins, S.A. Jaffer, T.F. Jaramillo et al., What would it take for renewably powered electrosynthesis to displace petrochemical processes? Science **364**(6438), 3506 (2019). https://doi.org/10.1126/science.aav3506
2. J. Li, S.U. Abbas, H. Wang, Z. Zhang, W. Hu, Recent advances in interface engineering for electrocatalytic CO_2 reduction reaction. Nano-Micro Lett. **13**, 216 (2021). https://doi.org/10.1007/s40820-021-00738-9
3. Z.Z. Wu, X.L. Zhang, Z.Z. Niu, F.Y. Gao, P.P. Yang et al., Identification of Cu(100)/Cu(111) interfaces as superior active sites for CO dimerization during CO_2 electroreduction. J. Am. Chem. Soc. **144**(1), 259–269 (2022). https://doi.org/10.1021/jacs.1c09508
4. X. Zheng, P.D. Luna, F.P.G. Arquer, B. Zhang, N. Becknell et al., Sulfur-modulated tin sites enable highly selective electrochemical reduction of CO_2 to formate. Joule **1**, 794–805 (2017). https://doi.org/10.1016/j.joule.2017.09.014
5. X. Lu, Y. Wu, X. Yuan, H. Wang, An integrated CO_2 electrolyzer and formate fuel cell enabled by a reversibly restructuring Pb-Pd bimetallic catalyst. Angew. Chem. Int. Ed. **58**(12), 4031–4035 (2019). https://doi.org/10.1002/anie.201814257
6. S. Zhao, S. Li, T. Guo, S. Zhang, J. Wang et al., Advances in Sn-based catalysts for electrochemical CO_2 reduction. Nano-Micro Lett. **11**, 62 (2019). https://doi.org/10.1007/s40820-019-0293-x
7. D. Wu, R. Feng, C. Xu, P.F. Sui, J. Zhang et al., Regulating the electron localization of metallic bismuth for boosting CO_2 electroreduction. Nano-Micro Lett. **14**, 38 (2021). https://doi.org/10.1007/s40820-021-00772-7
8. Q. Gong, P. Ding, M. Xu, X. Zhu, M. Wang et al., Structural defects on converted bismuth oxide nanotubes enable highly active electrocatalysis of carbon dioxide reduction. Nat. Commun. **10**, 2807 (2019). https://doi.org/10.1038/s41467-019-10819-4
9. C. Xia, P. Zhu, Q. Jiang, Y. Pan, W. Liang et al., Continuous production of pure liquid fuel solutions via electrocatalytic CO_2 reduction using solid-electrolyte devices. Nat. Energy **4**, 776–785 (2019). https://doi.org/10.1038/s41560-019-0451-x
10. F. Yang, A.O. Elnabawy, R. Schimmenti, P. Song, J. Wang et al., Bismuthene for highly efficient carbon dioxide electroreduction reaction. Nat. Commun. **11**, 1088 (2020). https://doi.org/10.1038/s41467-020-14914-9
11. P. Deng, F. Yang, Z. Wang, S. Chen, Y. Zhou et al., Metal-organic frameworks-derived carbon nanorods encapsulated bismuth oxides for rapid and selective CO_2 electroreduction to formate. Angew. Chem. Int. Ed. **59**(27), 10807–10813 (2020). https://doi.org/10.1002/anie.202000657
12. D.D. Zhu, J.L. Liu, S.Z. Qiao, Recent advances in inorganic heterogeneous electrocatalysts for reduction of carbon dioxide. Adv. Mater. **28**(18), 3423–3452 (2016). https://doi.org/10.1002/adma.201504766
13. C.W. Lee, J.S. Hong, K.D. Yang, K. Jin, J.H. Lee et al., Selective electrochemical production of formate from carbon dioxide with bismuth-based catalysts in an aqueous electrolyte. ACS Catal. **8**(2), 931–937 (2018). https://doi.org/10.1021/acscatal.7b03242
14. P. Deng, H. Wang, R. Qi, J. Zhu, S. Chen et al., Bismuth oxides with enhanced bismuth-oxygen structure for efficient electrochemical reduction of carbon dioxide to formate. ACS Catal. **10**(1), 743–750 (2019). https://doi.org/10.1021/acscatal.9b04043
15. T. Tran-Phu, R. Daiyan, Z. Fusco, Z. Ma, R. Amal et al., Nanostructured β-Bi_2O_3 fractals on carbon fibers for highly selective CO_2 electroreduction to formate. Adv. Funct. Mater. **30**(3), 1906478 (2019). https://doi.org/10.1002/adfm.201906478
16. S. Liu, X.F. Lu, J. Xiao, X. Wang, X.W.D. Lou, Bi_2O_3 nanosheets grown on multi-channel carbon matrix catalyze efficient CO_2 electroreduction to HCOOH. Angew. Chem. Int. Ed. **58**(39), 13828–13833 (2019). https://doi.org/10.1002/anie.201907674
17. Y. Zhang, X. Zhang, Y. Ling, F. Li, A.M. Bond et al., Controllable synthesis of few-layer bismuth subcarbonate by electrochemical exfoliation for enhanced CO_2 reduction performance. Angew. Chem. Int. Ed. **57**(40), 13283–13287 (2018). https://doi.org/10.1002/anie.201807466
18. B. Ravel, M. Newville, ATHENA, ARTEMIS, HEPHAESTUS: data analysis for X-ray absorption spectroscopy using IFEFFIT. J. Synchrotron Radiat. **12**, 537–541 (2005). https://doi.org/10.1107/S0909049505012719
19. C. Greaves, S.K. Blower, Structural relationships between $Bi_2O_2CO_3$ and β-Bi_2O_3. Mater. Res. Bull. **23**(7), 1001–1008 (1988). https://doi.org/10.1016/0025-5408(88)90055-4
20. G. Kresse, J. Hafner, Ab initio molecular dynamics for open-shell transition metals. Phys. Rev. B **48**(17), 13115–13118 (1993). https://doi.org/10.1103/PhysRevB.48.13115
21. G. Kresse, J. Furthmüller, Efficiency of ab-initio total energy calculations for metals and semiconductors using a plane-wave basis set. Comp. Mater. Sci. **6**(1), 15–50 (1996). https://doi.org/10.1016/0927-0256(96)00008-0
22. J.P. Perdew, K. Burke, M. Ernzerhof, Generalized gradient approximation made simple. Phys. Rev. Lett. **77**(18),

3865–3868 (1996). https://doi.org/10.1103/PhysRevLett.77.3865

23. G. Kresse, D. Joubert, From ultrasoft pseudopotentials to the projector augmented-wave method. Phys. Rev. B **59**(3), 1758–1775 (1999). https://doi.org/10.1103/PhysRevB.59.1758
24. A.A. Peterson, F. Abild-Pedersen, F. Studt, J. Rossmeisl, J.K. Nørskov, How copper catalyzes the electroreduction of carbon dioxide into hydrocarbon fuels. Energy Environ. Sci. **3**(9), 1311–1315 (2010). https://doi.org/10.1039/c0ee00071j
25. A.A. Peterson, J.K. Nørskov, Activity descriptors for CO_2 electroreduction to methane on transition-metal catalysts. J. Phys. Chem. Lett. **3**(2), 251–258 (2012). https://doi.org/10.1002/aenm.201903083
26. X. Tong, Z. Yang, J. Feng, Y. Li, H. Zhang, BiOCl/UiO-66 composite with enhanced performance for photo-assisted degradation of dye from water. Appl. Organomet. Chem. **32**(2), e4049 (2018). https://doi.org/10.1002/aoc.4049
27. J. Lu, W. Zhou, X. Zhang, G. Xiang, Electronic structures and lattice dynamics of layered BiOCl single crystals. J. Phys. Chem. Lett. **11**(3), 1038–1044 (2020). https://doi.org/10.1021/acs.jpclett.9b03575
28. W. Zhao, Y. Wang, A. Wang, J. Qian, W. Zhu et al., Novel $Bi_2O_2CO_3$/polypyrrole/*g*-C_3N_4 nanocomposites with efficient photocatalytic and nonlinear optical properties. RSC Adv. **7**(13), 7658–7670 (2017). https://doi.org/10.1039/c6ra28346b
29. G.E. Tobon-Zapata, S.B. Etcheverry, E.J. Baran, Vibrational spectrum of bismuth subcarbonate. J. Mater. Sci. Lett. **16**, 656–657 (1997). https://doi.org/10.1023/A:1018527602604
30. J.D. Grice, A solution to the crystal structures of bismutite and beyerite. Can. Mineral. **40**(2), 693–698 (2002). https://doi.org/10.2113/gscanmin.40.2.693
31. Z. Miao, Q. Wang, Y. Zhang, L. Meng, X. Wang, In situ construction of *S*-scheme AgBr/BiOBr heterojunction with surface oxygen vacancy for boosting photocatalytic CO_2 reduction with H_2O. Appl. Catal. B Environ. **301**, 120802 (2022). https://doi.org/10.1016/j.apcatb.2021.120802
32. H. Huang, K. Xiao, S. Yu, F. Dong, T. Zhang et al., Iodide surface decoration: a facile and efficacious approach to modulating the band energy level of semiconductors for high-performance visible-light photocatalysis. Chem. Commun. **52**(2), 354–357 (2016). https://doi.org/10.1039/c5cc08239k
33. S. Wei, H. Zhong, H. Wang, Y. Song, C. Jia et al., Oxygen vacancy enhanced visible light photocatalytic selective oxidation of benzylamine over ultrathin Pd/BiOCl nanosheets. Appl. Catal. B Environ. **305**, 121032 (2022). https://doi.org/10.1016/j.apcatb.2021.121032
34. A.K. Friedman, W. Shi, Y. Losovyj, A.R. Siedle, L.A. Baker, Mapping microscale chemical heterogeneity in nafion membranes with X-ray photoelectron spectroscopy. J. Electrochem. Soc. **165**(11), H733–H741 (2018). https://doi.org/10.1149/2.0771811jes
35. W. Cen, T. Xiong, C. Tang, S. Yuan, F. Dong, Effects of morphology and crystallinity on the photocatalytic activity of $(BiO)_2CO_3$ nano/microstructures. Ind. Eng. Chem. Res. **53**(39), 15002–15011 (2014). https://doi.org/10.1021/ie502670n
36. P. Kar, T.K. Maji, R. Nandi, P. Lemmens, S.K. Pal, In-situ hydrothermal synthesis of Bi-$Bi_2O_2CO_3$ heterojunction photocatalyst with enhanced visible light photocatalytic activity. Nano-Micro Lett. **9**, 18 (2017). https://doi.org/10.1007/s40820-016-0118-0
37. W. Ji, J. Niu, W. Zhang, X. Li, W. Yan et al., An electroactive ion exchange hybrid film with collaboratively-driven ability for electrochemically-mediated selective extraction of chloride ions. Chem. Eng. J. **427**, 130807 (2022). https://doi.org/10.1016/j.cej.2021.130807
38. N.E. Rajeevan, R. Kumar, D.K. Shukla, P. Thakur, N.B. Brookes et al., Bi-substitution-induced magnetic moment distribution in spinel $Bi_xCo_{2-x}MnO_4$ multiferroic. J. Phys. Condens. Matter **21**(40), 406006 (2009). https://doi.org/10.1088/0953-8984/21/40/406006
39. D.K. Shukla, R. Kumar, S. Mollah, R.J. Choudhary, P. Thakurm et al., Swift heavy ion irradiation induced magnetism in magnetically frustrated $BiMn_2O_5$ thin films. Phys. Rev. B **82**(17), 174432 (2010). https://doi.org/10.1103/PhysRevB.82.174432
40. R. Qiao, Y.D. Chuang, S. Yan, W. Yang, Soft X-ray irradiation effects of Li_2O_2, Li_2CO_3 and Li_2O revealed by absorption spectroscopy. PLoS ONE **7**(11), e49182 (2012). https://doi.org/10.1371/journal.pone.0049182
41. L. Wang, J. Han, Y. Zhu, R. Zhou, C. Jaye et al., Probing the dependence of electron transfer on size and coverage in carbon nanotube-quantum dot heterostructures. J. Phy. Chem. C **119**(47), 26327–26338 (2015). https://doi.org/10.1021/acs.jpcc.5b08681
42. Y. Ye, A. Kawase, M.K. Song, B. Feng, Y.S. Liu et al., X-ray absorption spectroscopy characterization of a Li/S cell. Nanomaterials **6**(1), 14 (2016). https://doi.org/10.3390/nano6010014
43. P.F. Liu, M.Y. Zu, L.R. Zheng, H.G. Yang, Bismuth oxyiodide microflower-derived catalysts for efficient CO_2 electroreduction in a wide negative potential region. Chem. Commun. **55**(82), 12392–12395 (2019). https://doi.org/10.1039/c9cc05089b
44. W. Lv, J. Bei, R. Zhang, W. Wang, F. Kong et al., $Bi_2O_2CO_3$ nanosheets as electrocatalysts for selective reduction of CO_2 to formate at low overpotential. ACS Omega **2**(6), 2561–2567 (2017). https://doi.org/10.1021/acsomega.7b00437
45. T. Cheng, C. Tan, S. Zhang, T. Tu, H. Peng et al., Raman spectra and strain effects in bismuth oxychalcogenides. J. Phys. Chem. C **122**(34), 19970–19980 (2018). https://doi.org/10.1021/acs.jpcc.8b05475
46. M. Zhang, W. Wei, S. Zhou, D.D. Ma, A. Cao et al., Engineering conductive network of atomically thin bismuthene with rich defects enables CO_2 reduction to formate with industry-compatible current densities and stability. Energy Environ. Sci. **14**, 4998–5008 (2021). https://doi.org/10.1039/d1ee01495a
47. N. Han, Y. Wang, H. Yang, J. Deng, J. Wu et al., Ultrathin bismuth nanosheets from in situ topotactic transformation for selective electrocatalytic CO_2 reduction to formate.

Nat. Commun. **9**, 1320 (2018). https://doi.org/10.1038/s41467-018-03712-z

48. T. Chen, T. Liu, T. Ding, B. Pang, L. Wang et al., Surface oxygen injection in tin disulfide nanosheets for efficient CO_2 electroreduction to formate and syngas. Nano-Micro Lett. **13**, 189 (2021). https://doi.org/10.1007/s40820-021-00703-6
49. C. Cao, D.D. Ma, J.F. Gu, X. Xie, G. Zeng et al., Metal-organic layers leading to atomically thin bismuthene for efficient carbon dioxide electroreduction to liquid fuel. Angew. Chem. Int. Ed. **132**(35), 15124–15130 (2020). https://doi.org/10.1002/anie.202005577
50. Y. Xing, X. Kong, X. Guo, Y. Liu, Q. Li et al., Bi@Sn core-shell structure with compressive strain boosts the electroreduction of CO_2 into formic acid. Adv. Sci. **7**(22), 1902989 (2020). https://doi.org/10.1002/advs.201902989
51. J.K. Norskov, T. Bligaard, J. Rossmeisl, C.H. Christensen, Towards the computational design of solid catalysts. Nat. Chem. **1**, 37–46 (2009). https://doi.org/10.1038/nchem.121

 https://doi.org/10.1007/s40820-022-00862-0